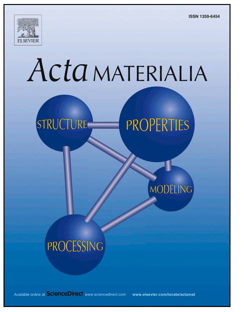

Mechanical properties in thermoelectric oxides: Ideal strength, deformation mechanism, and fracture toughness

Guodong Li, Umut Aydemir, Sergey I. Morozov, Samuel A. Miller, Qi An, William A. Goddard, III, Pengcheng Zhai, Qingjie Zhang, G. Jeffrey Snyder

PII: S1359-6454(18)30179-4

DOI: 10.1016/j.actamat.2018.02.063

Reference: AM 14418

To appear in: *Acta Materialia*

Received Date: 14 January 2018

Revised Date: 27 February 2018

Accepted Date: 28 February 2018

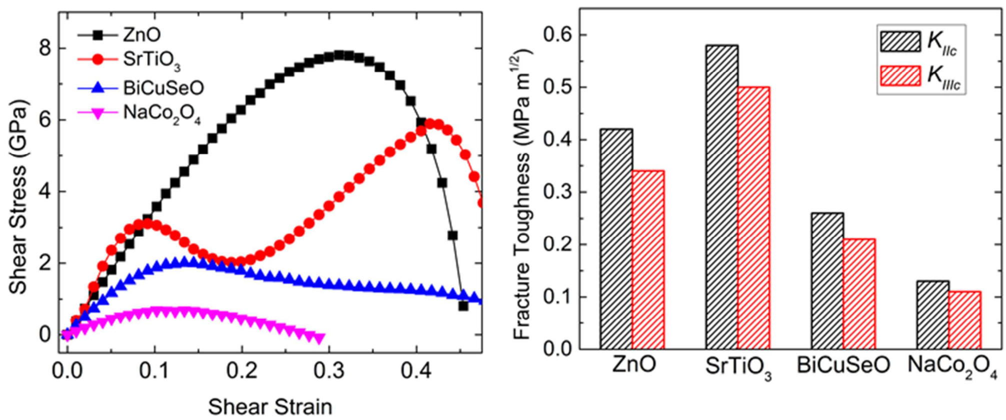
ZnO
SrTiO3
BiCuSeO
NaCo2O4
Shear Stress (GPa)
Shear Strain
0.0
0.1
0.2
0.3
0.4
0
2
4
6
8
Fracture Toughness (MPa m1/2)
KIIc
KIIIc
0.0
0.1
0.2
0.3
0.4
0.5
0.6
ZnO
SrTiO3
BiCuSeO
NaCo2O4

Mechanical Properties in Thermoelectric Oxides: Ideal Strength, Deformation Mechanism, and Fracture Toughness

Guodong Li [*,a,b], Umut Aydemir [b,c] Sergey I. Morozov [d], Samuel A. Miller [b], Qi An [e], William A. Goddard III [f], Pengcheng Zhai [a], Qingjie Zhang [*,a], and G. Jeffrey Snyder [b]

[a]State Key Laboratory of Advanced Technology for Materials Synthesis and Processing, Wuhan University of Technology, Wuhan 430070, China.

[b]Department of Materials Science and Engineering, Northwestern University, Evanston, Illinois 60208, USA.

[c]Department of Chemistry, Koc University, Sariyer, Istanbul 34450, Turkey

[d]Department of Computer Simulation and Nanotechnology, South Ural State University, Chelyabinsk 454080, Russia

[e]Department of Chemical and Materials Engineering, University of Nevada Reno, Reno, Nevada 89557

[f]Materials and Process Simulation Center, California Institute of Technology, Pasadena, California 91125, USA.

[*]Corresponding authors: guodonglee@whut.edu.cn; zhangqj@whut.edu.cn

Abstract: The recent dramatic improvements in high-performance thermoelectric (TE) oxides provide new exciting applications in the TE field, but the mechanical properties so important for engineering applications remain largely unexplored. Based on density functional theory (DFT) calculations, we report the ideal strength, deformation mechanism, and fracture toughness of such TE oxides as n-type ZnO and $SrTiO_3$ and p-type BiCuSeO and $NaCo_2O_4$. The Zn–O and Ti–O bonds forming the 3D Zn-O and Ti-O frameworks dominate the deformation and failure mechanisms of ZnO and $SrTiO_3$, respectively. Due to the higher stiffness of Ti-O octahedra compared with that of Zn-O tetrahedra, $SrTiO_3$ exhibits more robust macro-mechanical properties such as elastic modulus and fracture toughness than ZnO. The Bi–Se and Na–O bonds, which couple the different 2D substructures, are responsible for the relative slip in BiCuSeO and $NaCo_2O_4$, respectively. Since the Zn–O and Ti–O bonds are much stronger than the Bi–Se and Na–O bonds, we find that n-type ZnO and $SrTiO_3$ have a higher ideal strength and fracture toughness compared with p-type BiCuSeO and $NaCo_2O_4$. This work reveals that for TE module applications of oxides, it is most important to significantly improve the mechanical properties of the p-leg.

Keywords: Thermoelectric Oxides; Ideal Strength; Deformation Mechanism; Fracture Toughness

1. INTRODUCTION

The world's energy overconsumption, including the rapid depletion of fossil fuels, has led to severe environmental impacts on the global climate change. Thermoelectric (TE) energy conversion technology, which directly converts waste heat into electrical energy with no moving parts, could play a significant role in the solution for global sustainable energy [1-2]. However, engineering applications of TE materials lead to thermo-mechanical stresses that can cause crack or fatigue damage in TE materials, resulting in the failure of TE devices [3]. Consequently, it is essential to improve such mechanical properties as strength and fracture toughness for developing commercially viable TE devices.

The materials with the best TE properties are semiconductors containing such heavy (mostly toxic) elements as Bi, Pb, Sb, or Te [4-7], but these compounds are easily oxidized when subjected to air at high temperatures during heat recovery. Thus TE oxides exhibit better stability in ambient conditions, which enable the fabrication of more durable devices. The thermoelectric figure of merit (*zT*, $zT = \alpha^2 \sigma T / \kappa$, where α is the Seebeck coefficient, σ is the electrical conductivity, T is the temperature ,and κ is the thermal conductivity) of oxide materials has been remarkably enhanced within the last two decades [8-11], leading to values up to *zT* = 1.4 [11], but their mechanical properties are not well established, which limit their applications.

Efficient TE devices require both p- and n-type legs, preferably made of compatible materials with simultaneous high *zT* values and robust mechanical properties. The discovery of good 3D n-type oxides including doped $SrTiO_3$ based perovskites and ZnO, and promising p-type oxides such as layered BiCuSeO and $NaCo_2O_4$, has broken a new ground in the TE research field [8-11]. ZnO is a promising high *zT* material due to its high melting point, high electrical conductivity, and high Seebeck coefficient [12]. However, the thermal conductivity of ZnO (~40 W/mK for polycrystalline samples at 300 K [13]) is very high compared to other TE materials. Thus, the reduction of the thermal conductivity is essential for obtaining high *zT* values in n-type ZnO. Ohtaki *et al.* used Al and Ga co-doping to successfully reduce the thermal conductivity, obtaining *zT* = 0.65 at 1273 K for $Zn_{0.96}Al_{0.02}Ga_{0.02}O$, which is, to the best of our knowledge, the highest *zT* in bulk n-type oxides [14]. $SrTiO_3$ has received wide attention as a TE material because doped $SrTiO_3$ exhibits n-type conduction behavior with high carrier mobility and high power factor [15]. However, the observed high thermal conductivity due to its simple crystal structure limits the *zT* values to < 0.2 [10]. Through a nano-scale modulation doping strategy, Zhao *et al.* achieved a record high *zT* above 0.6 at 1000 - 1100 K in Nb-doped $SrTiO_3$ [16]. BiCuSeO is a potential p-type TE candidate exhibiting the highest *zT* value (~1.4) in oxides [11].

The intrinsically low thermal conductivity of BiCuSeO suggests that the most effective method to improve its *zT* value is enhancing the electrical transport properties, such as optimizing the carrier concentration through doping [17], increasing the carrier mobility through texturing [18], and band gap tuning [19]. Another layered p-type oxide material, $NaCo_2O_4$, also shows outstanding high TE performance, which is attributed to its high carrier concentration and low thermal conductivity [20]. An improvement of zT = 0.7-0.8 could be achieved for polycrystalline $NaCo_2O_4$ [21]. Although the TE properties have been markedly improved, the mechanical reliability of these promising oxides remains as a serious consideration for their practical applications. Unfortunately, the intrinsic mechanical properties, such as ideal strength, deformation mechanism, and fracture toughness of these oxide compounds remain unknown so far.

To predict the ideal strength, deformation and failure mechanism, and fracture toughness of n-type 3D (ZnO, $SrTiO_3$) and p-type 2D (BiCuSeO, and $NaCo_2O_4$) TE oxides, we used density functional theory (DFT) at the Perdew-Burke-Ernzerhof (PBE) functional level to examine their response under pure shear deformation.

- We find that n-type ZnO has the lowest ideal shear strength of 7.80 GPa along the (001)/<110> slip system, which leads to an estimated fracture toughness of K_{IIc} = 0.42 MPa $m^{1/2}$ and K_{IIIc} = 0.34 MPa $m^{1/2}$ based on its ideal stress-strain relation.
- The other n-type $SrTiO_3$ has its lowest ideal strength of 3.11 GPa along the (111)/<1-10> slip system with a fracture toughness of K_{IIc} = 0.58 MPa $m^{1/2}$ and K_{IIIc} = 0.50 MPa $m^{1/2}$.
- On the other hand, p-type BiCuSeO and $NaCo_2O_4$ have much lower ideal strengths of 2.0 GPa along the (001)/<100> and 0.69 GPa along the (001)/<110>, respectively, as well as much lower fracture toughness values of K_{IIc} of 0.26 and 0.13 MPa $m^{1/2}$.

We find that the ideal shear strength of n-type ZrO and $SrTiO_3$ are much higher than those of p-type BiCuSeO and $NaCo_2O_4$. We attribute this behavior to the more rigid Zn–O and Ti–O bonds based on higher calculated stretching force constants (SFC) of 5.63 eV/$Å^2$ for Zn–O and 5.43 eV/$Å^2$ for Ti–O, compared with the Bi–Se (SFC = 0.22 eV/$Å^2$) and Na–O bonds (SFC = 0.37 eV/$Å^2$). This work provides fundamental insights for understanding the deformation mechanism of TE oxides towards developing reliable and high-efficiency TE oxide devices.

2. METHODOLOGY

All DFT simulations were performed using the Vienna *ab initio* Simulation Package (VASP) plane wave periodic code [22-24]. The projector augmented wave (PAW) method and the Perdew-Burke-Ernzerhof (PBE) exchange-correlation functional were applied to account for the core-valence interactions [25]. The plane-wave cutoff energy was set to 500 eV in all the calculations, which gave excellent convergence on energy, force, stress, and geometries. The energy error for terminating electronic self-consistent field (SCF) and the force criterion for the geometry optimization were set equal to 1×10^{-6} eV and 1×10^{-2} eV/Å, respectively. Brillouin-zone integration was performed on Γ-centered symmetry reduced Monkhorst-Pack meshes with a fine resolution of $2\pi \times 1/40$ Å^{-1} for all calculations. The spin polarization was not considered here. The Electron localization function (ELF) value, which ranges from 0 to 1, was calculated to enable a reliable analysis of the bonding character and lone pair formation [26]. The elastic property is calculated using Voigt-Reuss-Hill method [27], and the shear deformation simulation is similar with our previous study [28]. They are explained in the supporting information (SI).

3. RESULTS AND DISCUSSION

3.1 Crystal structure and chemical bonding

ZnO crystallizes in hexagonal wurtzite structure (space group $P6_3mc$) which is the thermodynamically stable phase at ambient conditions. The unit cell contains 2 × Zn and 2 × O atoms where each Zn atom is tetrahedrally coordinated with O, as shown in Figure 1(a). The structure consists of a 3D framework of Zn-O with the bond length of 2.0 Å. The large Pauling electronegativity (EN) difference between Zn (χ_{Zn} = 1.65) and O (χ_O = 3.44) atoms indicates significant ionic bonding character, which is in agreement with the ELF isosurfaces localized around the oxygen atoms (Figure 1a). We calculate optimized lattice parameters of a = 3.29 Å and c = 5.31 Å, which are only 1.2% and 1.9% larger than the experimental values of a = 3.25 Å and c = 5.21 Å at 298K [29], and are in good agreement with the theoretical values of a = 3.28 Å and c = 5.30 Å from previous DFT calculations based on the PBE functional [30].

$SrTiO_3$ crystallizes in the cubic $Pm\bar{3}m$ perovskite structure with the Ti atoms located at the cube centers, the Sr atom at the corners and the O atom at the face centers (Figure 1(b)). Thus, Ti is octahedrally coordinated, while Sr is 12-fold coordinated with O atoms. The 3D framework has linear Ti-O-Ti connections with a Ti–O bond length of 1.98 Å. The EN difference of 1.90 between Ti (χ_{Ti} = 1.54) and O (χ_O = 3.44) is even slightly higher than the value (1.79) of Zn–O suggesting an ionic Ti–O interaction. Similarly to ZnO, ELF isosurfaces localized around the O atoms suggest that the interaction between Ti and O atoms is primarily ionic. Our optimized lattice parameter is *a* = 3.95 Å. This value is only 1.0% larger than the experimental value of 3.90 Å at 298K [31].

Layered BiCuSeO crystallizes in a ZrCuSiAs structure type with the space group $P4/nmm$. The structure consists of Bi-O layers alternately stacked with the isostructural Cu-Se layer along the *c*-axis (Figure 1(c)). The van der Waals-like Bi–Se interaction (d_{Bi-Se} = 3.27 Å) couples the Bi-O and the Cu-Se layers. The ELF maxima between cationic Bi^{2+} and anionic O^{2-} imply shared electrons between these atoms and a polar covalent bonding character of Bi–O bond (d_{Bi-O} = 2.34 Å) with an electronegativity difference of 1.42. This is similar to the covalent Cu–Se bond (d_{Cu-Se} = 2.53 Å) with a much lower electronegativity difference of 0.55. PBE gives equilibrium lattice parameters of *a* = 3.95 Å, *c* = 9.09 Å, which are only 0.5% and 1.8% larger than the experimental lattice parameters of *a* = 3.93 Å, *c* = 8.93 Å [11].

Layered $NaCo_2O_4$ has an orthorhombic unit cell with $Pmmn$ symmetry. The Na content is varied, which changes the crystal structure somewhat, but good TE properties are observed in stoichiometric $NaCo_2O_4$ [32]. The structure is schematically, as shown in Figure 1(d), with the Co-O layer and the Na layer stacked alternately along the *c*-axis. The ELF maxima between Co and O atoms within the Co-O layer indicate a polar covalent Co–O bonding character (d_{Co-O} =1.89 Å) with an electronegativity difference of 1.56, while the ELF local maxima around the O atom suggest lone pairs. The ionic Na–O interaction (d_{Na-O} = 2.34 or 2.46 Å) couples the Co-O and the Na layers, and the polar covalent Co–O bonding couples the Co-O layers. The unit cell contains 4 × Na, 8 × Co, and 16 × O atoms with the optimized lattice parameters of *a* = 4.90 Å, *b* = 5.66 Å, *c* = 11.04 Å. These values agree very well with the experimental lattice parameters of *a* = 4.88 Å, *b* = 5.63 Å, *c* = 11.13 Å [33].

3.2 Elastic mechanical properties

To provide basic information on the stability and rigidity of these oxide compounds, we computed the elastic properties including elastic constants (C_{ij}), bulk modulus (*B*), shear modulus (*G*), and Young's modulus (*E*). The predicted elastic mechanical properties are listed in Table 1, which agree reasonably well with previously reported *ab initio* and experimental results [30,34]. Since these oxides all contain such transition metals as Zn, Ti, Cu, and Co, we examined elastic properties of oxides using PBE+U (the *U* value is chosen from Refs [11, 35-37]), and found that the *U* correction plays a minor role in determining the mechanical properties. Due to the stronger 3D Zn-O and Ti-O frameworks, the elastic moduli of $SrTiO_3$ and ZnO are much larger than those of BiCuSeO and $NaCo_2O_4$ which have 2D layered frameworks. While the stretching force constant of Zn–O bonds (5.63 eV/ Å^2) is slightly larger than that for Ti–O bonds (5.43 eV/ Å^2), the greater number of bonds in $SrTiO_3$ (Ti-O octahedron) leads to larger elastic moduli (*B*, *G*, *E*) compared to ZnO (Zn-O tetrahedron). In 2D oxides, BiCuSeO and $NaCo_2O_4$ exhibit similar elastic properties. In all oxides, the shear modulus (*G)* is much lower than that of bulk modulus (*B)* and Young's modulus *E*, implying that shearing has a weaker resistance against external deformation compared to tension or compression. This suggests that shearing could play an important role in the deformation and failure mechanism of these oxides.

3.3 Deformation and failure mechanism

3.3.1 Shear-stress – shear-strain relationship of oxides

The ideal strength of a material is a fundamental mechanical property closely related to the nature of chemical bonding in a crystal [38]. The maximum stress at the stress-strain curve represents the theoretical strength only if any other instability does not occur prior to reaching the maximum, and the phonon spectra along the deformation path is sufficient to examine this structural instability [39-41]. The value of the ideal strength depends on the type of deformation, such as tension, compression, or shear. The predicted elastic properties above suggest that shear dominates the ideal strength and failure mechanisms.

To determine the ideal shear strength of oxides, we applied pure shear deformation along various slip systems of each compound to examine the shear response from the elastic region to the limit of the structural stability, as shown in Figures S1-S4 in the SI.

- For ZnO, the maximum stress for ideal shear deformation along the (001)/<110> is 7.80 GPa, which is lower than those shear along the (001)/<100> (7.82 GPa), (001)/<210> (8.85 GPa), and (101)/<110> (12.50 GPa) slip systems. This suggests that (001)/<110> is the least stress shear slip system for ZnO, indicating that it is the most likely failure slip system.
- In addition, (111)/<1-10>, (001)/<100>, and (001)/<110> slip systems are found to be the most likely plausible slip systems for $SrTiO_3$, BiCuSeO, and $NaCo_2O_4$, respectively, as shown in Figures S2-S4.

We summarize the shear-stress − shear-strain relationships for oxide compounds along their most plausible slip systems in Figure 2. Because the 3D frameworks in ZnO and $SrTiO_3$ are stronger than the 2D frameworks in BiCuSeO and $NaCo_2O_4$ (Figure 1), ZnO and $SrTiO_3$ have a higher ideal shear strength of 7.8 and 3.11 GPa, respectively, compared with those of BiCuSeO (2.0 GPa) and $NaCo_2O_4$ (0.69 GPa). The ideal shear strength of ZnO is higher than that of $SrTiO_3$, which is opposite the behavior of the shear modulus (*G*), as listed in Table 1. The ideal shear strength is the lowest value obtained for all possible shear directions, while the isotropic polycrystalline elastic moduli can be considered as the statistical mean quantity along all different directions. As shown in Figure S1 and S2, the lowest shear strength of $SrTiO_3$ is lower than that of ZnO, but the shear strengths of other shear systems in $SrTiO_3$ are much higher than those in ZnO. This leads to a much higher *G* in $SrTiO_3$ than ZnO. As shown in Figure 2, the structural stiffness starts to soften beyond the ideal strength point. In $SrTiO_3$, however, the shear stress starts to increase at 0.209 shear strain. This suggests that the structural rearrangement at this shear strain causes the structure to be further resistant to the shear deformation, which is similarly found in TiNiSn system [42].

3.3.2 Structure and bonding analysis

To determine the deformation and failure mechanisms of oxides, we extracted the atomic configurations and typical bond lengths to examine the bond-responding processes. Figure 3 displays the structural patterns of ZnO at several critical shear strains shearing along the least stress slip system of (001)/<110>. Figure 3(a) shows the intact structure highlighting the Zn-O hexagonal framework. As the system is sheared to 0.311 shear strain, which corresponds to the maximum shear stress of 7.80 GPa, the Zn-O hexagonal framework is distorted to resist the deformation (Figure 3(b)). The Zn1–O3 bond is stretched from 2.0 to 2.07 Å with a stretching ratio of 3.5%, and the Zn1–O2 bond is slightly stretched from 2.01 to 2.03 Å, accommodating the shear deformation. This different stretching ratio between the Zn1–O3 and Zn1–O2 bonds leads to the different reduction ratio between the O1–Zn1–O2 and O1–Zn1–O3 angles (Figure 3(d)), resulting in the distortion of the Zn-O hexagonal framework. The Zn1–O1 bond is first shrunk to suppress the structural stiffness softening, and then it is slightly stretched, as shown in Figure 3(d). As the shear strain increases to fracture strain of 0.434, the Zn1–O1 length is rapidly stretched to 2.16 Å with a stretching ratio of 8%, representing the highly softening or non-interaction of this bond and leading to the structural failure. This Zn1–O1 bond softening explains why the shear stress rapidly decreases from strain 0.311 to 0.434 (Figure 2). Moreover, the Zn-O framework changes to a pentagon shape with Zn1, O2, and O3 atoms in a same plane (Figure 3(c)). Therefore, the high ideal shear strength of ZnO arises from the compression of the Zn1–O1 bond which suppresses the softening of the structural rigidity. Beyond the maximum stress point, the rapid softening of the Zn1–O1 bond leads to stress relaxation and structural failure.

The structural changes of the other n-type oxide, $SrTiO_3$, at several critical shear strains along the least stress slip system of (111)/<1-10> are extracted, as shown in Figure 4. Figure 4(a) displays the intact structure highlighting the Ti–O cubic framework. When the shear strain increases to 0.092, corresponding to the ideal shear strength, the Ti1–O1 bond is stretched while the Ti2–O1 bond is shrunk uniformly accommodating the external deformation, because the Ti1, O1, and Ti2 atoms remain on a straight line (Figure 4(b)). The Ti2–O1–Ti3 bond angle is bent to resist the deformation. At the critical strain of 0.188, the highly softening or the breakage of the Ti1–O1 bond leads to the shear stress decreasing to a minimum value of 2.02 GPa (Figure 4(c)). Figure 4(d) displays the typical bond lengths (Ti1–O1 and Ti2–O1) and the bond angle (Ti2–O1–Ti3) against shear strain. The Ti2–O1 bond length decreases from 1.97 to 1.84 Å as the shear strain increases to 0.092, and the Ti2–O1–Ti3 angle decreases from 180° to 163°. The shrunk Ti2–O1 bond and the bent Ti2–O1–Ti3 angle suppress the structural stiffness softening, which is similarly found in ZnO. The Ti1–O1 bond increases to 2.37 Å with a large stretching ratio of 20.3%. Beyond the maximum stress point, the structural rigidity depends on the interplay between the Ti1–O1 bond softening and the Ti2–O1–Ti3 bond angle bending, where the Ti2–O1 bond has no contribution to the structural stiffness since the bond length remains unchanged. With increasing shear strain to 0.188, the Ti1–O1 bond is further stretched to 2.83 Å. This Ti1–O1 bond softening dominates the structural weakening effect, leading to the decreased shear stress against shear strain (Figure 2). However, with further increasing of the shear strain, the Ti2–O1–Ti3 angle bending dominates the structural stiffening effect, leading to the increased shear stress (Figure 2). Therefore, at 0.188 shear strain, the structural rearrangement results in a local minimum stress point in $SrTiO_3$ (Figure 2).

Figure 5 shows the structural changes of p-type layered oxide BiCuSeO at various shear strains shearing along the least stress slip system of (001)/<100>. Figure 5(a) shows the intact structure highlighting the alternately stacked Bi-O and Cu-Se substructures. Before the shear strain of 0.134, which corresponds to the maximum shear strength, the Cu-Se substructure is distorted to resist the deformation while the Bi-O substructure changes minimally. This leads to a relative slip between different Bi-O substructures as shown in Figure 5(b). With the shear strain increasing to 0.454, the Cu-Se substructure is highly distorted, leading to further slip between Bi-O layers (Figure 5(c)). This weakens the structural rigidity, resulting in the gradually released shear stress, as shown in Figure 2. Figure 5(d) plots the bond lengths of Bi1–Se1, Bi1–Se2 and the bond angles of Cu2–Se3–Cu1, Cu3–Se3–Cu1, O3–Bi1–O1, and O2–Bi1–O1 at various shear strains. The Bi1–Se1 bond is rapidly stretched and highly softened with increasing shear strain, which is responsible for the yielding stage beyond the ideal strength point (Figure 2). While the

Bi1–Se1 bond is shrunk resisting the shear deformation. These inconsistent bond deformations lead to the increase of the Cu2–Se3–Cu1 angle and the decrease of the Cu3–Se3–Cu1 angle, explaining why the Cu-Se layer was unsymmetrically distorted. In addition, the O3–Bi1–O1 and O2–Bi1–O1 bond angles are slightly increased from 73° to ~78° with nearly the same bending ratio during the entire shear process. This explains why the Bi-O layers hold together and slip relative to each other rather than deconstructing between layers.

Figure 6 shows the structural changes of the other p-type layered oxide $NaCo_2O_2$ at various shear strains shearing along its least stress slip system of (001)/<110>. As the system is sheared, the Na layer uniformly accommodates the shear deformation since the Na atoms are isolated along the Na layer (Na–Na length of 4.13 Å). Meanwhile, the Co-O layers remain intact due to the strong polar covalent interactions between Co and O atoms. This leads to a relative slip observed between the different Co-O substructures as shown in Figure 6(b) and 6(c), which is similarly found in the layered oxide BiCuSeO above. Figure 6(d) plots the bond lengths of Na1–O1 and Na1–O2 at various shear strains. These bond deformations are also similar with the Bi1–Se1 and Bi1–Se2 bonds in the layered BiCuSeO system as shown in Figure 5(d). The Na1–O1 bond is stretch with a much higher stretching ratio while the Na1–O2 bond is shrunk with a lower shrinking ratio resisting the deformation. At failure strain of 0.266, the Na1–O1 bond is stretched to 3.20 Å, indicating a highly softened or a broken bond. This totally releases the shear stress to zero and leads to the structural failure.

The ideal shear strength, which can be reliably determined by DFT calculations, has essential implications for the understanding of the mechanical behavior of a material at the limit of structural stability [38]. In these potential TE oxides, n-type ZnO and $SrTiO_3$ with the 3D frameworks have much stronger structural stability compared with p-type BiCuSeO and $NaCo_2O_4$ with the 2D frameworks. This leads to a much higher ideal strength observed in ZnO (7.80 GPa) and $SrTiO_3$ (3.11 GPa) compared with BiCuSeO (2.0 GPa) and $NaCo_2O_4$ (0.69 GPa). We calculated the bond stiffness in these oxide compounds to further understand how the structure influences the ideal shear strength. In n-type ZnO and $SrTiO_3$, the stretching force constant (SFC), which is calculated by the ATAT code [43], of Zn–O bond (d_{Zn-O} = 2.0 Å) and Ti–O bond (d_{Ti-O} = 1.97 Å) is 5.63 and 5.43 eV/Å^2, respectively. In p-type BiCuSeO and $NaCo_2O_4$, the SFC of the Bi–Se interaction (d_{Bi-Se} = 3.27 Å) and the Na–O interaction (d_{Na-O} = 2.46 Å) is only 0.22 and 0.37 eV/Å^2, respectively. This quantitatively explains why n-type 3D ZnO and $SrTiO_3$ are much more robust than p-type 2D BiCuSeO and $NaCo_2O_4$. This trend is similarly observed in our previous results on other non-oxide high performance TE semiconductors such as 3D TiNiSn [42] and $CoSb_3$ [28], and 2D SnSe [44], Mg_3Sb_2 [45], and Bi_2Te_3 [46]. In 3D ZnO and $SrTiO_3$, although the Ti-O octahedron in $SrTiO_3$ (6 Ti–O bonds) contains more bonds compared with the Zn-O tetrahedron in ZnO (4 Zn–O bonds), the directional plane-shearing leads to a much lower ideal shear strength (3.11 GPa) of $SrTiO_3$ along (111)/<1-10> compared with that (7.80 GPa) of ZnO along (001)/<110>. In 2D BiCuSeO and $NaCo_2O_4$, although the coupling interaction of Na–O in $NaCo_2O_4$ (0.37 eV/Å^2) is a little stronger than that of the Bi–Se (0.22 eV/Å^2) in BiCuSeO, the stiffness of Na layers consisting of isolated Na atoms in $NaCo_2O_4$ is much weaker than that of the Bi-O or Cu-Se layer in BiCuSeO. This leads to a lower ideal shear strength of $NaCo_2O_4$ (0.69 GPa) compared with that of BiCuSeO (2.0 GPa).

3.4 Fracture toughness from ideal stress-strain calculations

Fracture toughness (K_c), which describes the ability of a material containing a crack to resist fracture, is one of the most important properties of a material for many design applications [47]. The ideal shear stress-strain relations (Figure 2) can be utilized to predict the fracture toughness for mode II (K_{IIc}) and III (K_{IIIc}) loading conditions (see Figure 7 (a)-(b)). Fracture toughness K_{Ic} (mode I) would be estimated from the tensile-stress – tensile-strain relations, which were not computed in this paper. For mode II in the plane strain condition, the fracture toughness is derived [48]:

$$K_{IIc}^2 = \frac{2S_{IIc}G}{1-v} \qquad \text{Eqn. 1}$$

and from similar arguments, the mode III fracture toughness:

$$K_{IIIc}^2 = 2S_{IIIc}G \qquad \text{Eqn. 2}$$

Where G is the shear modulus (Table 1) and v is Poisson's ratio which can be calculated by $v = \frac{3B-2G}{2(3B+G)}$ [27]. $S_{IIc} = S_{IIIc} = \gamma_{us}$ is called the unstable stacking energy, which corresponds approximately to the energy required to nucleate a full dislocation (edge in mode II and screw in mode III). γ_{us}, which is given by the area under the ideal engineering shear stress-displacement curves, can be calculated by integrating the ideal engineering shear stress-displacement curves. The detailed estimation method is illustrated in the SI.

Figure 7(c) plots the predicted fracture toughness of ZnO, $SrTiO_3$, BiCuSeO, and $NaCo_2O_4$. Since flawless crystals are used for the calculations, the predicted fracture toughness is the possible upper limit of experiments. The n-type ZnO and $SrTiO_3$ with the 3D frameworks have a higher fracture toughness compared with the p-type BiCuSeO and $NaCo_2O_4$ with the 2D frameworks, which is in agreement with the structural stiffness discussion in the previous section. In 3D oxides, due to the high stiffness of Ti-O octahedron and large elastic properties in $SrTiO_3$, $SrTiO_3$ exhibits a higher fracture toughness (K_{IIc} = 0.58 MPa $m^{1/2}$ and K_{IIIc} = 0.50 MPa $m^{1/2}$) compared with ZnO (K_{IIc} = 0.42 MPa $m^{1/2}$ and K_{IIIc} = 0.34 MPa $m^{1/2}$). In 2D oxides, due to the weak stiffness of the Na layer and low ideal strength in $NaCo_2O_4$, $NaCo_2O_4$ shows a much lower fracture toughness (K_{IIc} = 0.13 MPa $m^{1/2}$ and K_{IIIc} = 0.11 MPa $m^{1/2}$) compared with BiCuSeO (K_{IIc} = 0.26 MPa $m^{1/2}$ and K_{IIIc} = 0.21 MPa $m^{1/2}$). As shown in Figure 7(c), for commercial realization of TE oxides, the fracture toughness of p-type 2D oxide BiCuSeO and $NaCo_2O_4$ should be enhanced.

The fracture toughness estimation verifies that the investigation of the ideal stress-strain relations at the atomic scale can be used to rationally design the macroscopic mechanical properties, which is beneficial for the development of robust oxide TE materials for the engineering application of oxide TE devices.

4. CONCLUSIONS

We applied DFT to determine the ideal shear strength, deformation mechanism, and fracture toughness of oxide compounds under pure shear deformation. For n-type high-performance oxides ZnO and $SrTiO_3$, the softening of the Zn–O and Ti–O bonds leads to a decreased structural stiffness of 3D Zn-O and Ti-O frameworks, respectively, as well as the stress relaxation. $SrTiO_3$ exhibits more robust macro-mechanical properties such as elastic modulus and fracture toughness than ZnO, because the stiffness of Ti-O octahedra in $SrTiO_3$ is much stronger than that of Zn-O tetrahedra in ZnO. For p-type BiCuSeO and $NaCo_2O_4$, the softening of the Cu–Se and Na–O bonds creates pathways to slip between different substructures, which releases the stress and results in the structural failure. Due to a much higher SFC of the Zn–O and Ti–O bonds compared with the Cu–Se and Na–O bonds, n-type ZnO and $SrTiO_3$ are found to have much higher ideal strength and fracture toughness than p-type BiCuSeO and $NaCo_2O_4$. For commercial applications of oxide thermoelectrics, the weak structural stiffness of p-type 2D oxide BiCuSeO and $NaCo_2O_4$ should be improved to improve their mechanical strength.

Supporting Information: Explanation on how we calculate the elastic constants and stress-strain relations; The shear-stress−shear-strain relationships for oxide compounds (ZnO, $SrTiO_3$, BiCuSeO, and $NaCo_2O_4$) under shear deformation along various slip systems; Prediction of fracture toughness from ideal shear-stress – shear-strain curves.

ACKNOWLEDGEMENTS

This work is partially supported by NSF of China under No. 51772231, the 111 Project of China under Project no. B07040. S.A.M was supported by National Science Foundation DMR program under grant no. 1334713, 1334351, and 1333335. Q.A was supported by the National Science Foundation CMMI program under grant no. 1727428. S.M. was thankful for the support by Act 211 Government of the Russian Federation, uner No. 02.A03.21.0011 and by the Supercomputer Simulation Laboratory of South Ural State University [49].

REFERENCES

[1] Snyder, G. J.; Toberer, E. S. Complex Thermoelectric Materials. *Nat. Mater.* **2008**, 7, 105-114.

[2] He, J.; Tritt, T. M., Advances in Thermoelectric Materials Research: Looking Back and Moving Forward. *Science.* **2017**, *357*, 1369.

[3] Barako, M. T.; Park, W.; Marconnet, A. M.; Asheghi, M.; Goodson, K. E., Thermal Cycling, Mechanical Degradation, and the Effective Figure of Merit of a Thermoelectric Module. *J. Electron. Mater.* **2013**, *42*, 372-381.

[4] Pei, Y.; Shi, X.; LaLonde, A.; Wang, H.; Chen, L.; Snyder, G. J., Convergence of Electronic Bands for High Performance Bulk Thermoelectrics. *Nature.* **2011,** 473, 66-69.

[5] Tang, Y. L.; Gibbs, Z. M.; Agapito, L. A.; Li, G.; Kim, H. S.; Nardelli, M. B.; Curtarolo, S.; Snyder, G. J., Convergence of Multi-Valley Bands as the Electronic Origin of High Thermoelectric Performance in $CoSb_3$ Skutterudites. *Nat. Mater.* **2015**, 14, 1223-1228.

[6] Zhao, L. D.; Lo, S. H.; Zhang, Y.; Sun, H.; Tan, G.; Uher, C.; Wolverton, C.; Dravid, V. P.; Kanatzidis, M. G., Ultralow Thermal Conductivity and High Thermoelectric Figure of Merit in SnSe Crystals. *Nature,* **2014,** *508*, 373-377.

[7] Kim, S. I.; Lee, K. H.; Mun, H. A.; Kim, H. S.; Hwang, S. W.; Roh, J. W.; Yang, D. J.; Shin, W. H.; Li, X. S.; Lee, Y. H.; Snyder, G. J.; Kim, S. W., Dense Dislocation Arrays Embedded in Grain Boundaries for High-Performance Bulk Thermoelectrics. *Science*, **2015**, 348, 109-114.

[8] He, J.; Liu, Y.; Funahashi, R., Oxide thermoelectrics: The challenges, Progress, and Outlook. *J. Mater. Res.* **2011,** *26* (15), 1762-1772.

[9] Fergus, J. W., Oxide Materials for High Temperature Thermoelectric Energy Conversion. *J. Eur. Ceram. Soc.* **2012**, 32 (3), 525-540.

[10] Ohtaki, M., Recent Aspects of Oxide Thermoelecric Materials for Power Generation from Mid-to-High Temperature Heat Source. *J. Ceram. Soc. Japan.* **2011**, 119, 770-775.

[11] Zhao, L. D.; He, J.; Berardan, D.; Lin, Y.; Li, J.-F.; Nan, C.-W.; Dragoe, N., BiCuSeO Oxyselenides: New Promising Thermoelectric Materials. *Energy Environ. Sci.* **2014**, 7 (9), 2900-2924.

[12] Ohtaki, M.; Tsubota, T.; Eguchi, K.; Arai, H., High-Temperature Thermoelectric Properties of $(Zn_{1-x}Al_x)O$. *J. Appl. Phys.* **1996**, 79 (3), 1816-1818.

[13] Tsubota, T.; Ohtaki, M.; Eguchi, K.; Arai, H., Thermoelectric Properties of Al-Doped ZnO as a Promising Oxide Material for High-Temperature Thermoelectric Conversion. *J. Mater. Chem.* **1997**, 7 (1), 85-90.

[14] Ohtaki, M.; Araki, K.; Yamamoto, K., High Thermoelectric Performance of Dually Doped ZnO Ceramics. *J. Electron. Mater.* **2009**, 38 (7), 1234-1238.

[15] Okuda, T.; Nakanishi, K.; Miyasaka, S.; Tokura, Y., Large Thermoelectric Response of Metallic Perovskites: $Sr_{1-x}La_xTiO_3$ ($0 <= x <= 0.1$). *Phys. Rev. B.* **2001**, 63 (11), 113104.

[16] Wang, J.; Zhang, B.-Y.; Kang, H.-J.; Li, Y.; Yaer, X.; Li, J.-F.; Tan, Q.; Zhang, S.; Fan, G.-H.; Liu, C.-Y.; Miao, L.; Nan, D.; Wang, T.-M.; Zhao, L.-D., Record High Thermoelectric Performance in Bulk $SrTiO_3$ via Nano-Scale Modulation Doping. *Nano Energy.* **2017,** *35*, 387-395.

[17] Tan, S. G.; Lei, H. C.; Shao, D. F.; Lv, H. Y.; Lu, W. J.; Huang, Y. N.; Liu, Y.; Yuan, B.; Zu, L.; Kan, X. C.; Song, W. H.; Sun, Y. P., Enhanced Low Temperature Thermoelectric Performance of Ag-Doped BiCuSeO. *Appl. Phys. Lett.* **2014**, 105 (8), 082109.

[18] Li, F.; Li, J. F.; Zhao, L. D.; Xiang, K.; Liu, Y.; Zhang, B. P.; Lin, Y. H.; Nan, C. W.; Zhu, H. M., Polycrystalline BiCuSeO Oxide as a Potential Thermoelectric Material. *Energy Environ. Sci.* **2012**, 5 (5), 7188-7195.

[19] Liu, Y.; Lan, J. L.; Xu, W.; Liu, Y. C.; Pei, Y. L.; Cheng, B.; Liu, D. B.; Lin, Y. H.; Zhao, L. D., Enhanced Thermoelectric Performance of a BiCuSeO System via Band Gap Tuning. *Chem. Commun.* **2013**, 49 (73), 8075-8077.

[20] Terasaki, I.; Sasago, Y.; Uchinokura, K., Large Thermoelectric Power in $NaCo_2O_4$ Single Crystals. *Phys. Rev. B.* **1997**, 56 (20), 12685-12687.

[21] Ito, M.; Nagira, T.; Furumoto, D.; Katsuyama, S.; Nagai, H., Synthesis of $Na_xCo_2O_4$ Thermoelectric Oxides by the Polymerized Complex Method. *Scripta. Mater.* **2003**, 48 (4), 403-408.

[22] Kresse, G.; Furthmuller, J. Efficiency of ab-initio Total Energy Calculations for Metals and Semiconductors Using a Plane-Wave Basis Set. *Comp. Mater. Sci.* **1996**, 6, 15-50.

[23] Kresse, G.; Furthmuller, J. Efficient Iterative Schemes for ab initio Total-Energy Calculations Using a Plane-Wave Basis Set. *Phys. Rev. B.* **1996**, 54, 11169-11186.

[24] Kresse, G.; Joubert, D. From Ultrasoft Pseudopotentials to the Projector Augmented-Wave Method. *Phys. Rev. B.* **1999**, 59, 1758-1775.

[25] Perdew, J.; Burke, K.; Ernzerhof, M. Generalized Gradient Approximation Made Simple. *Phys. Rev. Lett.* **1996**, 77, 3865–3868.

[26] Silvi, B.; Savin, A., Classification of Chemical Bonds Based on Topological Analysis of Electron Localization Functions. *Nature*. **1994**, *371*, 683−686.

[27] Chung, D. H. Elastic Moduli of Single-Crystal and Polycrystalline MgO. *Philos. Mag.* **1963**, 8, 833-841.

[28] Li, G. D.; An, Q.; Li, W. J.; Goddard, W. A.; Zhai, P. C.; Zhang, Q. J.; Snyder, G. J., Brittle Failure Mechanism in Thermoelectric Skutterudite $CoSb_3$. *Chem. Mater.* **2015**, *27*, 6329-6336.

[29] Schulz, H.; Thiemann, K. H., Structure Parameters and Polarity of the Wurtzite Type Compounds Sic-2H and ZnO. *Solid. State. Commun.* **1979**, 32 (9), 783-785.

[30] de Jong, M.; Chen, W.; Angsten, T.; Jain, A.; Notestine, R.; Gamst, A.; Sluiter, M.; Krishna Ande, C.; van der Zwaag, S.; Plata, J. J.; Toher, C.; Curtarolo, S.; Ceder, G.; Persson, K. A.; Asta, M., Charting the Complete Elastic Properties of Inorganic Crystalline Compounds. *Sci. data.* **2015**, 2, 150009.

[31] Abramov, Y. A.; Tsirelson, V. G.; Zavodnik, V. E.; Ivanov, S. A.; Brown, I. D., The Chemical Bond and Atomic Displacements in $SrTiO_3$ from X-Ray Diffraction Analysis. *Acta. Crystallogr. B.* **1995,** *51*, 942-951.

[32] Koumoto, K.; Terasaki, I.; Funahashi, R., Complex Oxide Materials for Potential Thermoelectric Applications. *MRS. Bull*. **2006,** *31* (3), 206-210.

[33] Huang, Q.; Foo, M. L.; Lynn, J. W.; Zandbergen, H. W.; Lawes, G.; Wang, Y. Y.; Toby, B. H.; Ramirez, A. P.; Ong, N. P.; Cava, R. J., Low Temperature Phase Transitions and Crystal Structure of $Na_{0.5}CoO_2$. *J. Phys: Condens. Mat.* **2004,** *16* (32), 5803-5814.

[34] Wang, G.; Li, X., Size Dependency of the Elastic Modulus of ZnO Nanowires: Surface Stress Effect. *Appl. Phys. Lett.* **2007,** *91* (23), 231912.

[35] Özgür, Ü.; Alivov, Y. I.; Liu, C.; Teke, A.; Reshchikov, M. A.; Doğan, S.; Avrutin, V.; Cho, S. J.; Morkoç, H., A Comprehensive Review of ZnO Materials and Devices. *J. Appl. Phys.* **2005,** *98* (4), 041301.

[36] Cuong do, D.; Lee, B.; Choi, K. M.; Ahn, H. S.; Han, S.; Lee, J., Oxygen Vacancy Clustering and Electron Localization in Oxygen-Deficient SrTiO(3): LDA+U Study. *Phys. Rev. Lett.* **2007**, 98 (11), 115503.

[37] Wang, Y.; Ni, J., Effect of Electronic Correlation on the Na Ordering of Na_xCoO_2. *J. Phys: Condens. Mat.* **2007**, 19 (8), 086203.

[38] Ogata, S.; Li, J.; Yip, S., Ideal pure shear strength of aluminum and copper. *Science* **2002,** *298* (5594), 807-811.

[39] Clatterbuck, D. M.; Krenn, C. R.; Cohen, M. L.; Morris, J. W., Phonon instabilities and the ideal strength of aluminum. *Phys. Rev. Lett.* **2003,** *91* (13), 135501.

[40] Dubois, S. M. M.; Rignanese, G. M.; Pardoen, T.; Charlier, J. C., Ideal strength of silicon: An ab initio study. *Phys. Rev. B.* **2006,** *74* (23), 235203.

[41] Rehak, P.; Cerny, M.; Sob, M., Mechanical stability of Ni and Ir under hydrostatic and uniaxial loading. *Model. Simul. Mater. Sci.* **2015,** *23* (5), 055010.

[42] Li, G.; An, Q.; Aydemir, U.; Goddard III, W. A.; Wood, M.; Zhai, P.; Zhang, Q.; Snyder, G. J., Enhanced Ideal Strength of Thermoelectric Half-Heusler TiNiSn by Sub-Structure Engineering. *J. Mater. Chem. A* **2016,** *4*, 14625-14636.

[43] Walle, A.; Asta, M.; Ceder, G., The Alloy Theoretic Automated Toolkit: A User Guide. *Calphad.* **2002**, *26*, 539-553.

[44] Li, G.; Aydemir, U.; Wood, M.; Goddard, W. A. III.; Zhai, P.; Zhang, Q.; Snyder, G. J., Ideal Strength and Deformation Mechanism in High-Efficiency Thermoelectric SnSe. *Chem. Mater.* **2017**, 29, 2382-2389.

[45] Li, G.; Aydemir, U.; Wood, M.; An, Q.; Goddard Iii, W. A.; Zhai, P.; Zhang, Q.; Snyder, G. J., Deformation Mechanisms in High-Efficiency Thermoelectric Layered Zintl Compounds. *J. Mater. Chem. A* **2017,** *5* (19), 9050-9059.

[46] Li, G.; Aydemir, U.; Morozov, S. I.; Wood, M.; An, Q.; Zhai, P. C.; Zhang, Q. J.; Goddard, W. A.; Snyder, G. J., Superstrengthening Bi_2Te_3 through Nanotwinning. *Phys Rev Lett* **2017**, 119 (8), 085501.

[47] Chantikul, P.; Anstis, G. R.; Lawn, B. R.; Marshall, D. B., A Critical-Evaluation of Indentation Techniques for Measuring Fracture-Toughness .2. Strength Method. *J. Am. Ceram. Soc.* **1981,** *64* (9), 539-543.

[48] Rice, J. R., Dislocation Nucleation from a Crack Tip: an Analysis based on the Peierls Concept. *J. Mech. Phys. Solids.* **1992**, *40*, 239-271.

[49] Kostenetskiy, P. S.; and Safonov, A.Y., SUSU Supercomputer Resources. Proceedings of the 10th Annual International Scientific Conference on Parallel Computing Technologies (Arkhangelsk, Russia, 2016).

Table:

Table 1. Predicted elastic constants (C_{ij}) and other related elastic properties: bulk modulus (*B*), shear modulus (*G*), and Young's modulus (*E*) of ZnO, $SrTiO_3$, BiCuSeO, and $NaCo_2O_4$ compounds. All values given in units of GPa and a comparison with previous *ab-initio* and experimental results is provided.

Compound	Method	C_{11}	C_{12}	C_{13}	C_{22}	C_{23}	C_{33}	C_{44}	C_{66}	*B*	*G*	*E*
ZnO	Our PBE	191.5	108.7	95.0	191.4	95.0	206.7	41.4	38.0	131.9	45.5	122.5
	PBE+U	221.1	105.9	87.4	221.1	87.4	234.3	57.6	53.4	137.6	63.4	164.9
	PBE[30]	188	109	92	188	92	205	37	39	130	41	111.3
	Expt[34]											118
$SrTiO_3$	Our PBE	333.3	103.2	103.2	333.3	103.2	333.3	107.3	107.3	179.9	110.3	274.8
	PBE+U	321.4	97.3	97.3	321.4	97.3	321.4	104.6	104.6	172.0	107.5	266.9
	PBE[30]	319	100	100	319	100	319	110	110	173	110	272.3
BiCuSeO	Our PBE	143.0	60.76	56.8	143.0	56.8	96.0	40.2	26.5	79.5	34.6	90.6
	PBE+U	146.3	63.2	54.6	146.3	54.6	100.1	41.2	26.1	80.2	35.3	92.3
$NaCo_2O_4$	Our PBE	261.5	84.5	10.1	273.8	16.0	96.2	91.4	20.6	81.4	45.9	115.9
	PBE+U	265.6	90.0	31.6	251.2	28.6	124.6	83.4	21.7	95.9	45.9	118.7

Figure Captions:

Figure 1. Crystal structure and chemical bonding of promising oxide TE materials: (a) ZnO (with calculated isosurfaces at a value of 0.7 of ELF) (b) $SrTiO_3$ (0.65) (c) BiCuSeO (0.9) (d) $NaCo_2O_4$ (0.7).

Figure 2. The shear-stress−shear-strain relationships for oxide compounds along their most plausible slip systems. In these oxides, the most plausible slip system for ZnO, $SrTiO_3$, BiCuSeO, and $NaCo_2O_4$ is (001)/<110>, (111)/<1-10>, (001)/<100>, and (001)/<110>, respectively.

Figure 3. The atomic structures of n-type 3D ZnO shearing along the least stress slip system of (001)/<110>: (a) Intact structure prepared to shear, (b) Atomic structure at 0.311 shear strain corresponding to the maximum stress point, (c) Atomic structure at failure strain of 0.434, (d) The typical bond lengths (Zn1–O1, Zn1–O2, Zn1–O3) and the bond angles (O1–Zn1–O2 and O1–Zn1–O3) with the increasing shear strain along the (001)/<110> slip system.

Figure 4. The atomic structures of n-type 3D oxide $SrTiO_3$ shearing along the least stress slip system of (111)/<1-10>: (a) Intact structure prepared to shear, (b) Atomic structure at 0.092 shear strain corresponding to the maximum stress point, (c) Atomic structure at 0.188 shear strain corresponding to the structural rearrangement, (d) The typical bond lengths (Ti1–O1 and Ti1–O2) and the bond angle (Ti3–O2–Tι2) with the increasing shear strain along the (111)/<1-10> slip system.

Figure 5. The atomic structures of p-type layered BiCuSeO shearing along the least stress slip system of (001)/<100>: (a) Intact structure prepared to shear, (b) Atomic structure at 0.134 shear strain corresponding to the maximum stress point, (c) Atomic structure at 0.454 shear strain, (d) The typical bond lengths (Bi1–Se1 and Bi1–Se2) and the bond angles (Cu2–Se3–Cu1, Cu3–Se3–Cu1, O3–Bi1–O1, and O2–Bi1–O1) with the increasing shear strain along the (001)/<100> slip system. The red dashed lines displayed in Figure 5(a)-(c) show the slip of layered Bi-O substructures.

Figure 6. The atomic structures of n-type layered oxide $NaCo_2O_4$ shearing along the least stress slip system of (001)/<110>: (a) Intact structure prepared to shear, (b) Atomic structure at 0.102 shear strain corresponding to the maximum stress point, (c) Atomic structure at 0.266 shear strain, (d) The typical bond lengths (Na1–O1 and Na1–O2) with the increasing shear strain along the (001)/<110> slip system. The black dashed lines displayed in Figure 6(a)-(c) show the slip of layered Co-O substructures.

Figure 7. Fracture toughness estimations for ZnO, $SrTiO_3$, BiCuSeO, and $NaCo_2O_4$ oxide compounds. Schematic illustration showing the loading geometries corresponding to the respective fracture toughness estimations: (a) K_{IIc}, and (b) K_{IIIc} (Source: https://commons.wikimedia.org/w/index.php?curid=3429474). (c) Predicted fracture toughness from ideal shear-stress – shear-strain curves.

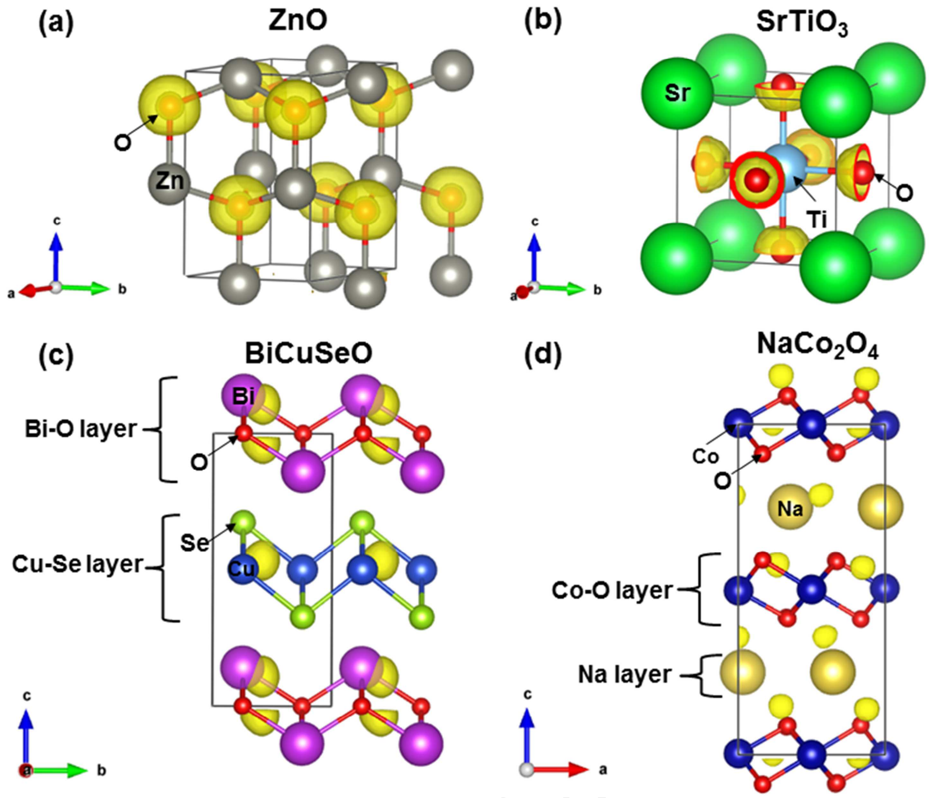
(a)
ZnO
O
Zn
(b)
SrTiO3
Sr
Ti
O
(c)
BiCuSeO
Bi-O layer
Bi
O
Cu-Se layer
Se
Cu
(d)
NaCo2O4
Co
O
Na
Co-O layer
Na layer

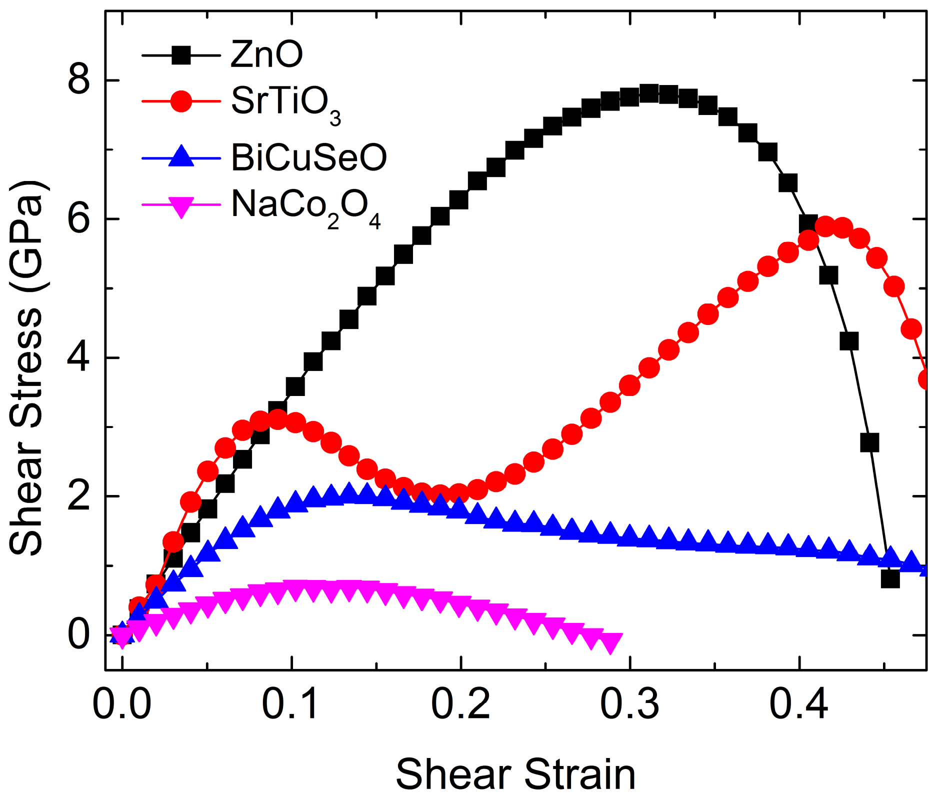
ZnO
SrTiO3
BiCuSeO
NaCo2O4
Shear Stress (GPa)
0
2
4
6
8
0.0
0.1
0.2
0.3
0.4
Shear Strain

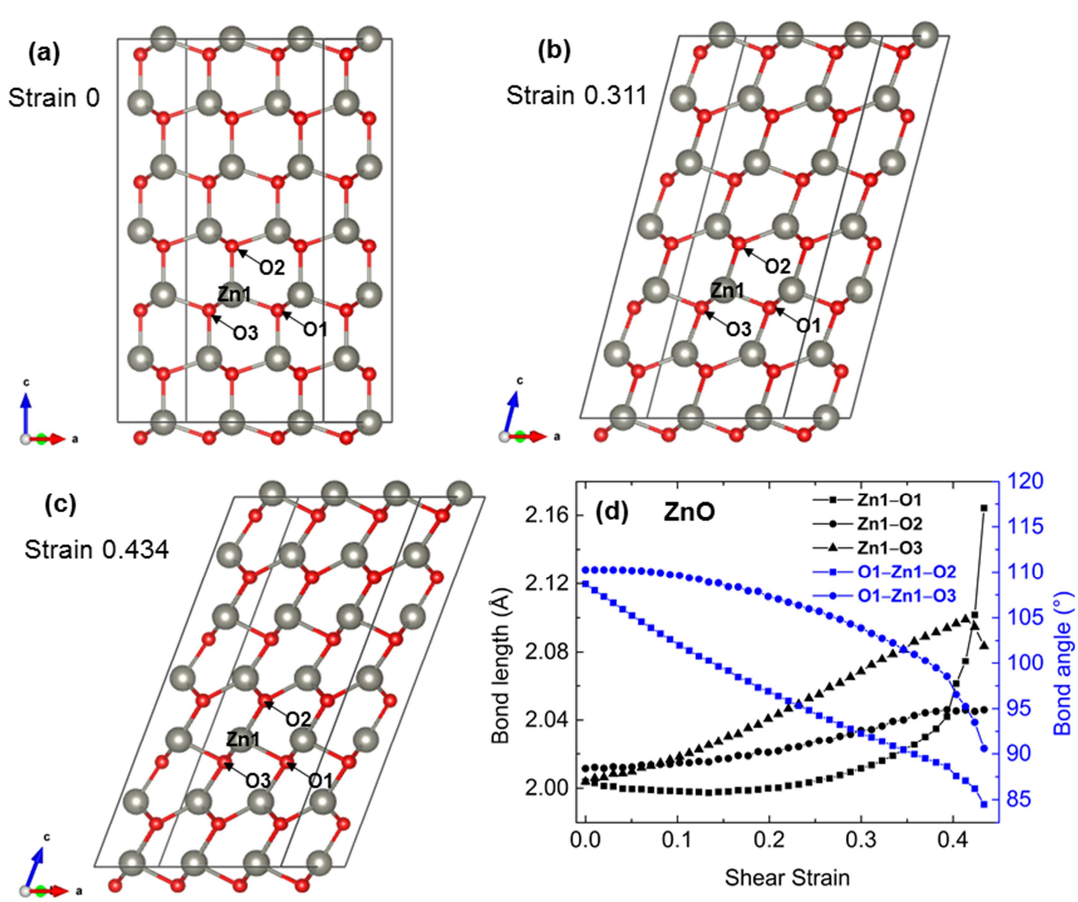
(a)
Strain 0
O2
Zn1
O3
O1
(b)
Strain 0.311
O2
Zn1
O3
O1
(c)
Strain 0.434
O2
Zn1
O3
O1
(d) ZnO
Zn1–O1
Zn1–O2
Zn1–O3
O1–Zn1–O2
O1–Zn1–O3
Bond length (Å)
Bond angle (°)
Shear Strain
c
a

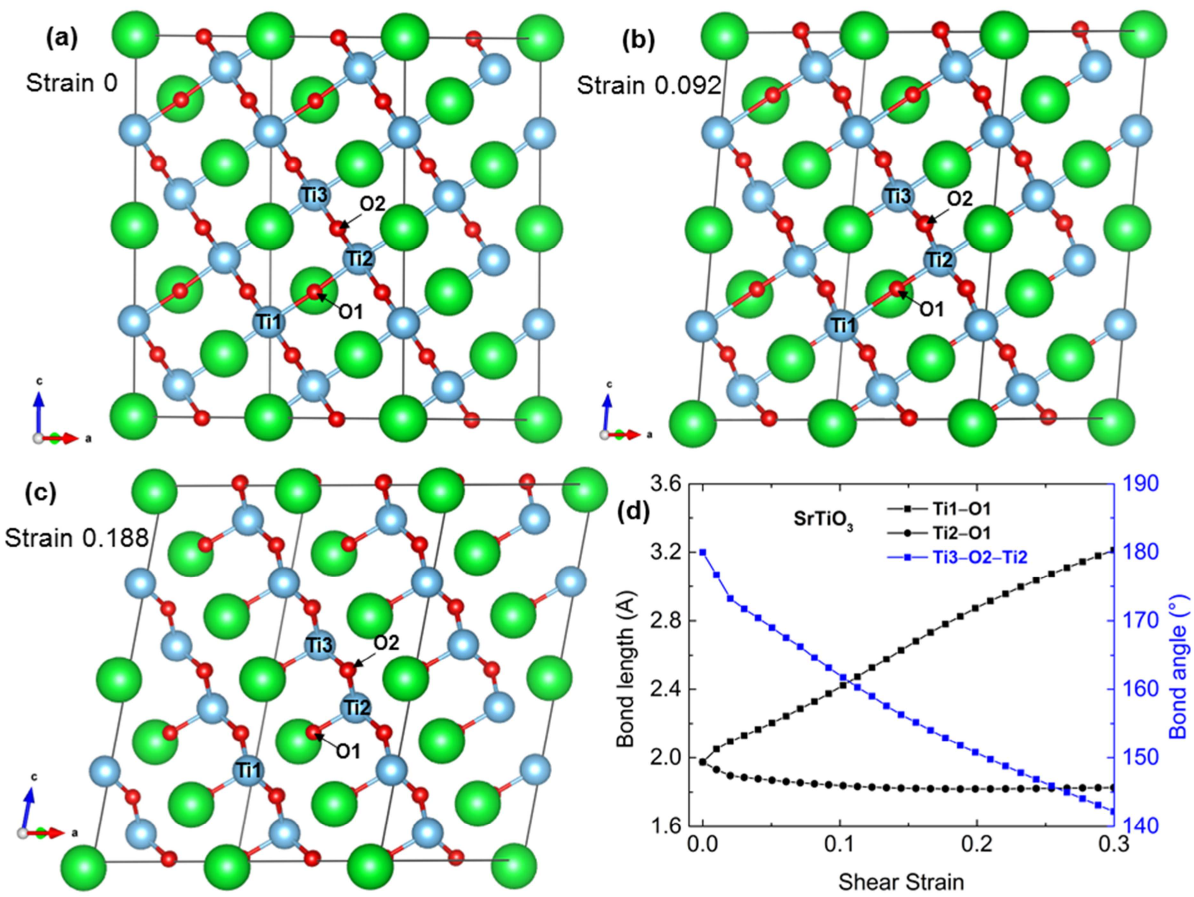
(a)
Strain 0
Ti3
O2
Ti2
Ti1
O1
(b)
Strain 0.092
Ti3
O2
Ti2
Ti1
O1
(c)
Strain 0.188
Ti3
O2
Ti2
Ti1
O1
(d)
SrTiO3
Ti1–O1
Ti2–O1
Ti3–O2–Ti2
Bond length (A)
Bond angle (°)
Shear Strain
3.6
3.2
2.8
2.4
2.0
1.6
190
180
170
160
150
140
0.0
0.1
0.2
0.3

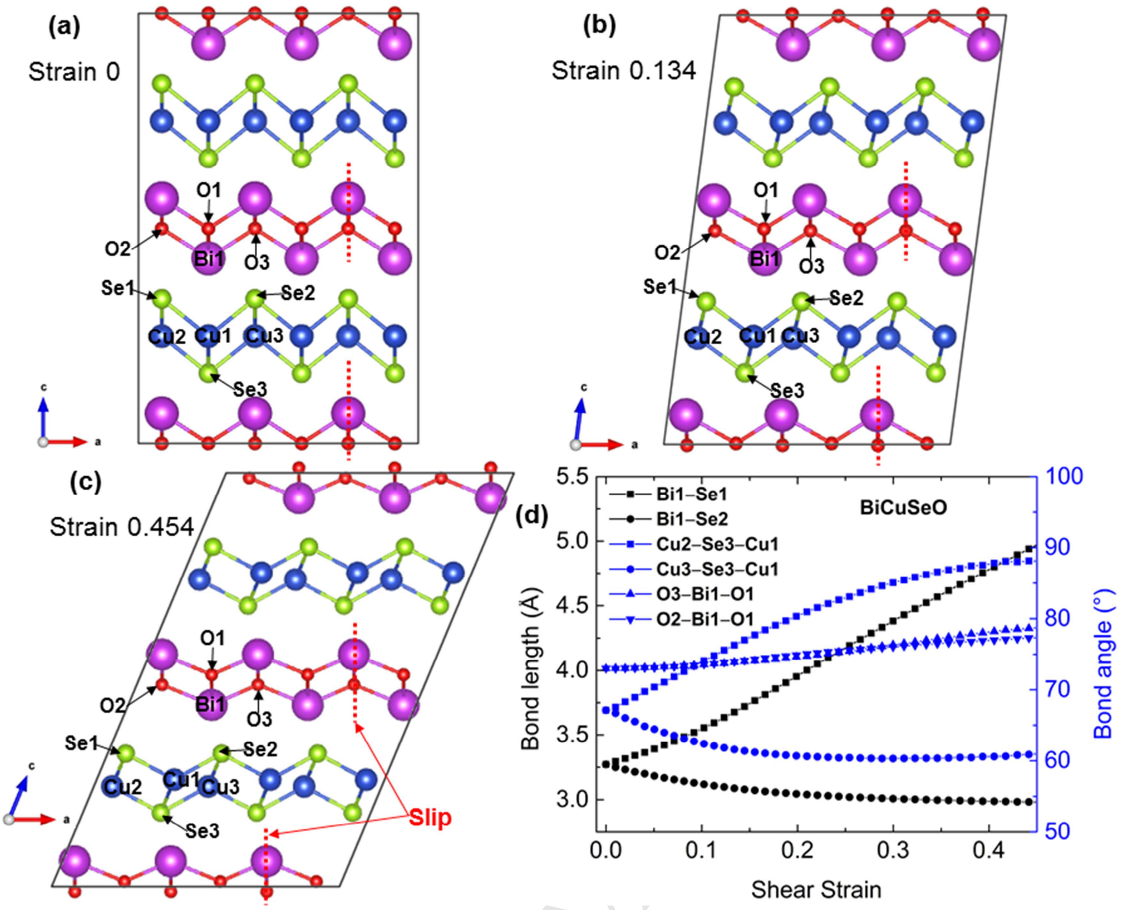
(a)
Strain 0
O1
O2
Bi1
O3
Se1
Se2
Cu2
Cu1
Cu3
Se3
(b)
Strain 0.134
(c)
Strain 0.454
Slip
(d)
Bi1–Se1
Bi1–Se2
Cu2–Se3–Cu1
Cu3–Se3–Cu1
O3–Bi1–O1
O2–Bi1–O1
BiCuSeO
Bond length (Å)
Bond angle (°)
Shear Strain

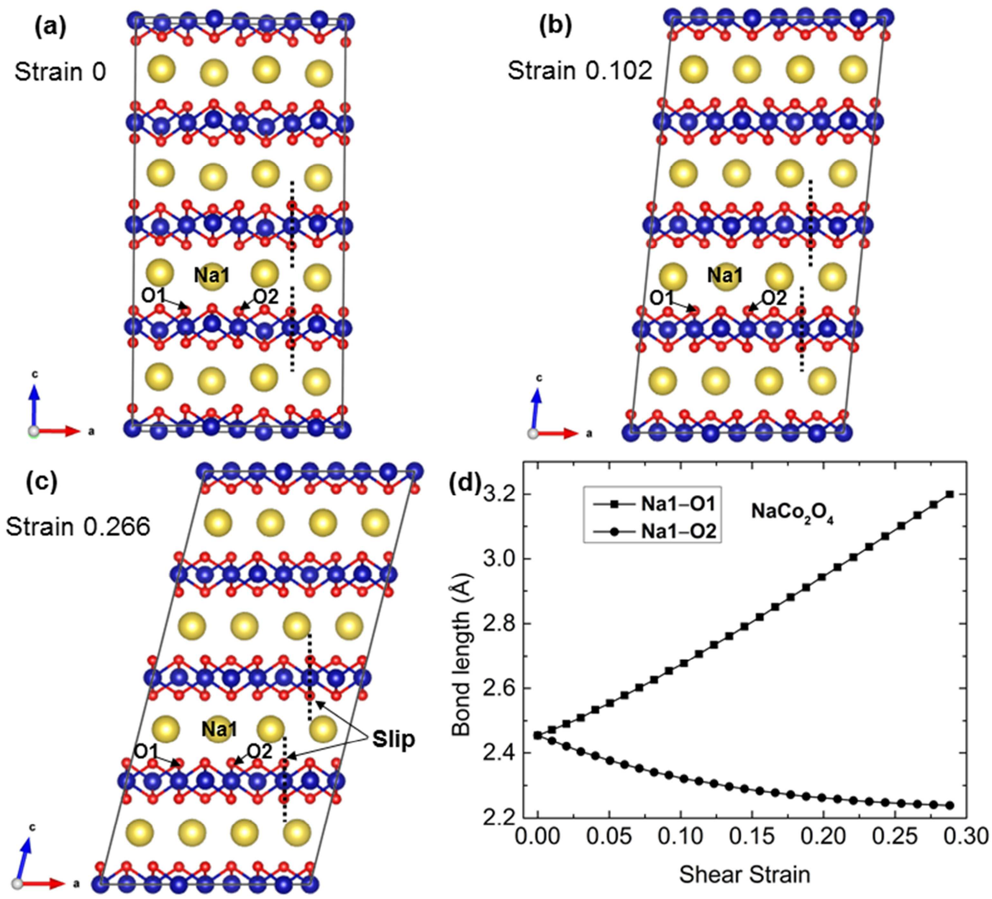
(a)
Strain 0
Na1
O1
O2
(b)
Strain 0.102
Na1
O1
O2
(c)
Strain 0.266
Na1
O1
O2
Slip
(d)
Na1–O1
Na1–O2
NaCo2O4
Bond length (Å)
Shear Strain
3.2
3.0
2.8
2.6
2.4
2.2
0.00
0.05
0.10
0.15
0.20
0.25
0.30

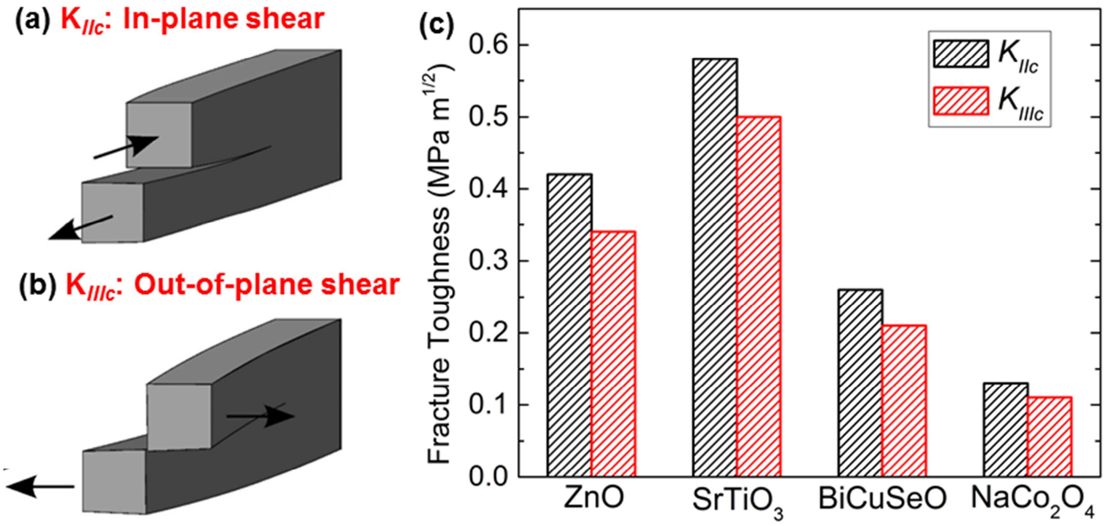
(a) K_IIc: In-plane shear
(b) K_IIIc: Out-of-plane shear
(c)
Fracture Toughness (MPa m^1/2)
0.0
0.1
0.2
0.3
0.4
0.5
0.6
K_IIc
K_IIIc
ZnO
SrTiO3
BiCuSeO
NaCo2O4

Supporting Information

Mechanical Properties in Thermoelectric Oxides: Ideal Strength, Deformation Mechanism, and Fracture Toughness

Guodong Li [*,a,b], Umut Aydemir [b,c] Sergey I. Morozov [d], Samuel A. Miller [b], Qi An [e], William A. Goddard III [f], Pengcheng Zhai [a], Qingjie Zhang [*,a], and G. Jeffrey Snyder [b]

[a]State Key Laboratory of Advanced Technology for Materials Synthesis and Processing, Wuhan University of Technology, Wuhan 430070, China.

[b]Department of Materials Science and Engineering, Northwestern University, Evanston, Illinois 60208, USA.

[c]Department of Chemistry, Koc University, Sariyer, Istanbul 34450, Turkey

[d]Department of Computer Simulation and Nanotechnology, South Ural State University, Chelyabinsk 454080, Russia

[e]Department of Chemical and Materials Engineering, University of Nevada Reno, Reno, Nevada 89557

[f]Materials and Process Simulation Center, California Institute of Technology, Pasadena, California 91125, USA.

[*]Corresponding authors: guodonglee@whut.edu.cn; zhangqj@whut.edu.cn

Explanation on how we calculate the elastic constants and stress-strain relations

The elastic constants, C_{ij}, were computed from stress - strain relationship as a function of various cell distortions, δ ($\delta < 3\%$), starting with our optimized atomic structure. The stiffness constant, S_{ij}, was derived from $S_{ij} = (C_{ij})^{-1}$. Subsequently, the Voigt-Reuss-Hill method was applied to calculate the isotropic polycrystalline elastic moduli from the calculated single-crystal elastic and stiffness constants.

To determine the ideal shear strength and the failure mechanism of these oxides, we achieved quasi-static mechanical loading by imposing a shear strain along one particular shear direction while allowing full structural relaxation along the other five strain components. The residual stresses are all less than 0.2 GPa for all pure shear deformations. The computed stress-strain relations are true stress-strain relations.

The shear-stress−shear-strain relationships for n-type 3D ZnO oxide compound under shear deformation along various slip systems

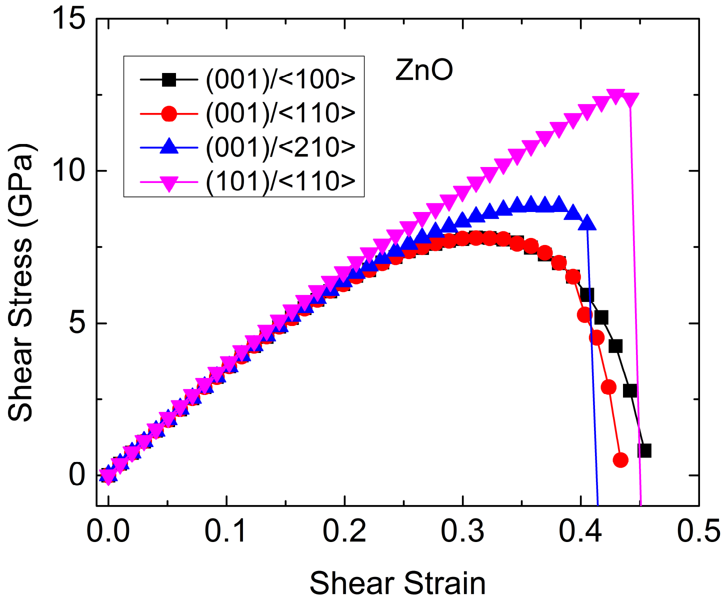

Figure S1. The shear-stress−shear-strain relationships for ZnO oxide compound under shear deformation along various slip systems. Shearing along the (001)/<110> is found to have the lowest ideal strength of 7.80 GPa. This suggests that (001)/<110> is the most plausible slip system to be activated under pressure. The (001)/<100> slip system has slightly higher ideal shear strength than (001)/<110>.

The shear-stress−shear-strain relationships for n-type 3D $SrTiO_3$ oxide compound under shear deformation along various slip systems

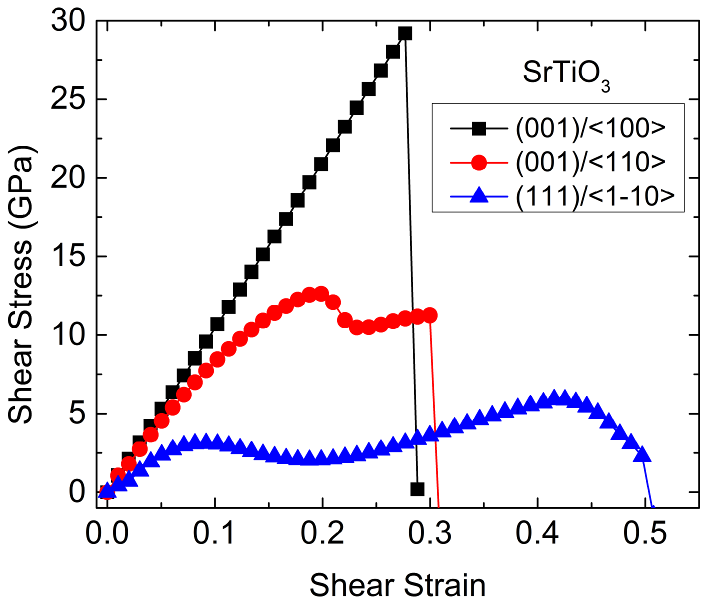

Figure S2. The shear-stress−shear-strain relationships for $SrTiO_3$ oxide compound under shear deformation along various slip systems. The directional slip leads to a much weaker structural stiffness along (111)/<1-10> compared with that along (001)/<100>. This leads to a much lower ideal strength (3.11 GPa) of (111)/<1-10> compared with that (29.19 GPa) of (111)/<1-10>. Shearing along the (111)/<1-10> is found to have the lowest ideal strength of 3.11 GPa. This suggests that (111)/<1-10> is the most plausible slip system to be activated under pressure.

The shear-stress−shear-strain relationships for p-type 2D BiCuSeO oxide compound under shear deformation along various slip systems

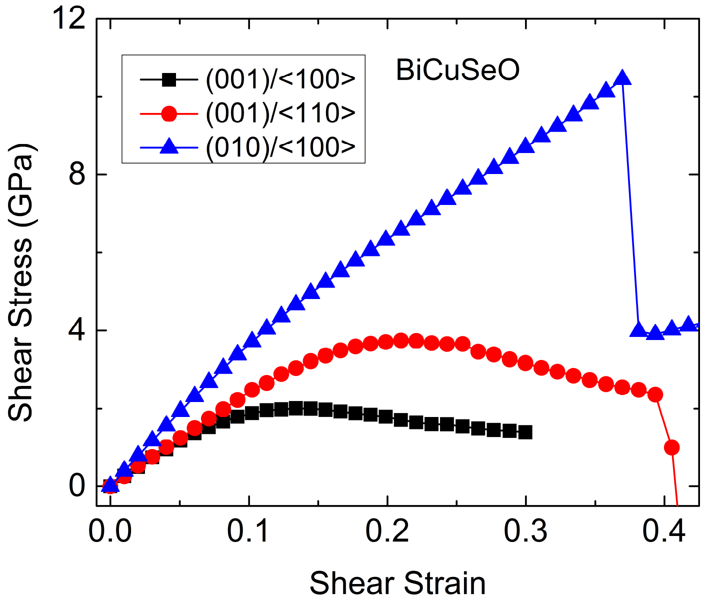

Figure S3. The shear-stress−shear-strain relationships for BiCuSeO oxide compound under shear deformation along various slip systems. Shearing along the (001)/<100> is found to have the lowest ideal strength of 2.0 GPa. This suggests that (001)/<100> is the most plausible slip system to be activated under pressure.

The shear-stress−shear-strain relationships for p-type 2D $NaCo_2O_4$ oxide compound under shear deformation along various slip systems

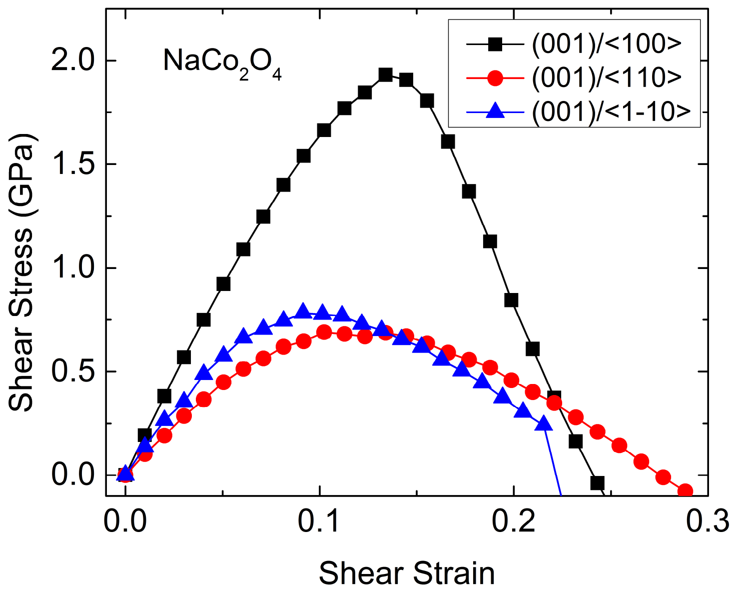

Figure S4. The shear-stress−shear-strain relationships for $NaCo_2O_4$ oxide compound under shear deformation along various slip systems. Shearing along the (001)/<110> is found to have the lowest ideal strength of 0.69 GPa. This suggests that (001)/<110> is the most plausible slip system to be activated under pressure.

Prediction of fracture toughness from ideal shear-stress – shear-strain curves

The ideal shear-stress – shear-strain curves shown in Fig. 2 are computed as a true-stress (σ_t) and true-strain (ε_t). This should be converted to an engineering stress (σ_e) and engineering strain (ε_e) for the integral, which can be accomplished by the relations:

$$\varepsilon_t = \ln(1+\varepsilon_e) \qquad \text{Eqn. S1}$$

$$\sigma_t = \sigma_e \exp(\varepsilon_t) \qquad \text{Eqn. S2}$$

The engineering displacement (Δd_e) is then calculated from the engineering strain by:

$$\Delta d_e = \varepsilon_e c_0 \qquad \text{Eqn. S3}$$

where c_0 is the optimized lattice parameter along the *c*-axis direction of the shear system.

Using the relations listed above, the curves shown in Figure 2 can be converted to ideal engineering stress-displacement. The maximum displacement was found by linearly extrapolating the engineering stress to zero from the right-most tail of the data. The $G_{IIc} = G_{IIIc} = \gamma_{us}$ values were calculated for these oxides by integrating the ideal engineering shear stress-displacement curves. Using the elastic mechanical properties listed in Table 1, Eqn. 1-2 was used to estimate fracture toughness, which is shown in Figure 7(c).